Complex dynamics of long, flexible fibers in shear

John LaGrone [a,*], Ricardo Cortez [a], Wen Yan [b], Lisa Fauci [a]

[a] Department of Mathematics, Tulane University, New Orleans, LA 70118, United States
[b] Flatiron Institute, Simons Foundation, New York, NY 10010, United States

ABSTRACT

The macroscopic properties of polymeric fluids are inherited from the material properties of the fibers embedded in the solvent. The behavior of such passive fibers in flow has been of interest in a wide range of systems, including cellular mechanics, nutrient acquisition by diatom chains in the ocean, and industrial applications such as paper manufacturing. The rotational dynamics and shape evolution of fibers in shear depends upon the slenderness of the fiber and the non-dimensional "elasto-viscous" number that measures the ratio of the fluid's viscous forces to the fiber's elastic forces. For a small elasto-viscous number, the nearly-rigid fiber rotates in the shear, but when the elasto-viscous number reaches a threshold, buckling occurs. For even larger elasto-viscous numbers, there is a transition to a "snaking behavior" where the fiber remains aligned with the shear axis, but its ends curl in, in opposite directions. These experimentally-observed behaviors have recently been characterized computationally using slender-body theory and immersed boundary computations. However, classical experiments with nylon fibers and recent experiments with actin filaments have demonstrated that for even larger elasto-viscous numbers, multiple buckling sites and coiling can occur. Using a regularized Stokeslet framework coupled with a kernel independent fast multipole method, we present simulations that capture these complex fiber dynamics.

1. Introduction

The motion of flexible fibers in flow is central to many biological systems at the microscale. Mammalian sperm flagella propel these cells through the female reproductive tract [4], while microtubule fibers are ingredients of the mitotic spindle in cell division [22]. While the dynamics of these fiber-fluid systems are actuated by molecular motors, other biological systems contain passive fibers that are transported and undergo shape deformations due to the flow. Examples of these passive fibers include microtubules transported by cytoplasmic streaming in fungal hyphae [19] and chains of diatom cells that move with water currents through the ocean [9].

Early experiments by Forgacs and Mason [6] on synthetic fibers in shear demonstrated a spectrum of orbits and shape deformations. Shorter, stiffer fibers experienced a signature Jeffery orbit, where periodic tumbling was accompanied by little to no deformation. Longer fibers exhibited periodic orbits with shape deformations that were qualitatively catalogued as *S*-turns (buckling) and snake turns. For the longest fibers, Forgacs and Mason [6] observed complex shape deformations that they described as coiled orbits with entanglement. Decades later, with the availability of microfluidic technology, these periodic shape deformations in shear have been observed in DNA strands and actin filaments [7,8,14]. Most recently, the complex coiling and entanglement of long actin fibers was measured experimentally in [13], where an actin filament of length of more than sixty microns was subjected to a shear

flow. A fiber that is initially straight and aligned with the shear direction develops the shape of a hook at the ends of the fiber during a snake turn. Later in time, the fiber exhibits a more complex behavior, including multiple buckling sites in the middle of the fiber and three-dimensional entanglement.

In a review article on the dynamics of flexible fibers in flow, du Roure et al. [3] describe recent technological advances in experimentation and recent algorithmic advances in computational modeling that have given rise to deeper understanding and probing of fiber-fluid systems. Exploiting the inertia-free environment at the microscale, and the slender geometry of the fibers, much progress has been made in using slender body theory [20] to describe the orbits and buckling of fibers in flow e.g., [14,16,21,24]. Kuei et al. [10] have modeled a fiber as a string of spherical beads subjected to a shear flow, and simulations exhibit complex coiling and, in some cases, production of knots. In this manuscript, we present a mathematical model and numerical method that captures the dynamics of short fibers as well as the complex shape deformations of the longest fibers without asymptotic restrictions on the slenderness that are typical of a slender body formulation. The fibers we consider are represented by a discretization of their surface. We use a similar fiber model as that used to examine the dynamics of diatom chains in a non-zero Reynolds number environment [17]. However, here we assume that the length and velocity scales are small enough so that the fluid dynamics is well-described by the Stokes equations, and use a regularized Stokeslet formulation [1,2] of the fluid-fiber system.

While the diatom chain model of Nguyen and Graham [17] was able to capture complex buckling behavior of long fibers, it was based on an adaptive mesh immersed boundary method that needed fine grid reso-

lution on the fluid domain near the fiber. In contrast, the regularized Stokeslet formulation described here, while requiring fine resolution of the fiber surface to capture the complex behavior, is based on fundamental solutions of the Stokes equations and does not require a spatial grid on the surrounding fluid. Although one of the most attractive features of the regularized Stokeslet framework is the ease of implementation – the velocities at N nodes are computed based upon the forces at each of the N nodes - the direct N^2 evaluation becomes costly for N large. In order to resolve the surface of a long, thin fiber using a discretization such that the distance between nodes around a cross section is on the order of the distance between cross sections, the number of nodes N becomes necessarily large. Here we demonstrate that the incorporation of a kernel independent fast multipole method [28] to compute velocities rather than a direct evaluation allows for faster simulations of the longest fibers, and will be a promising tool for multi-fiber investigations.

In the following sections we will discuss the construct of the model fiber and its coupling to a Stokes fluid using the method of regularized Stokeslets. We will demonstrate the shape deformations of fibers of increasing length in shear, and discuss how these results compare with recent studies. Moreover, we will present simulations of long fibers (at large elasto-viscous numbers) that capture the complex coiling and entanglement observed in experiments.

2. Methodology

2.1. Stokes equations

Assuming that length and time scales are small, we model a flexible fiber coupled to a viscous fluid in three dimensions by the incompressible Stokes equations:

$$0 = -\nabla \hat{P} + \mu \Delta \hat{\mathbf{u}} + \hat{\mathbf{F}},$$
$$0 = \nabla \cdot \hat{\mathbf{u}}, \tag{1}$$

where $\hat{P}$ is the pressure, $\hat{\mathbf{u}}$ is the fluid velocity, μ is the fluid viscosity, and $\hat{\mathbf{F}}$ is the external force per volume exerted by the fiber on the fluid. The forces in Eq. (1) are localized at the fiber surface, and will be described below. The motion of the passive fiber will be driven by an imposed background shear flow $\hat{\mathbf{u}}_b(\hat{x}, \hat{y}, \hat{z}) = (\dot{\gamma}\hat{y}, 0, 0)$.

We use a regularized Stokeslet framework [1] to model the elastohydrodynamic system. Rather than using a surface integral of Dirac delta function forces $A(\mathbf{y})\hat{\mathbf{f}}(\mathbf{y})\delta(\mathbf{x} - \mathbf{y})$, we consider regularized force density $A(\mathbf{y})\hat{\mathbf{f}}(\mathbf{y})\phi_\varepsilon(\mathbf{x} - \mathbf{y})$ supported on a patch of area $A(\mathbf{y})$ on the surface of the fiber. The regularization (or blob) function is chosen to be:

$$\phi_\varepsilon(\mathbf{x} - \mathbf{y}) = \frac{15\varepsilon^4}{8\pi(r^2 + \varepsilon^2)^{7/2}}, \tag{2}$$

where $r = \|\mathbf{x} - \mathbf{y}\|$, and ε is the regularization parameter [1]. This leads to the velocities due to the regularized Stokeslets as follows:

$$\mathbf{u}_{st}(\mathbf{x}) = \int_\Sigma S_\varepsilon(\mathbf{x}, \mathbf{y})\hat{\mathbf{f}}(\mathbf{y}) dS_y$$
$$= \frac{1}{8\pi\mu} \int_\Sigma \frac{(r^2 + 2\varepsilon^2)\hat{\mathbf{f}}(\mathbf{y}) + (\hat{\mathbf{f}}(\mathbf{y}) \cdot (\mathbf{x} - \mathbf{y}))(\mathbf{x} - \mathbf{y})}{(r^2 + \varepsilon^2)^{3/2}} dS_y, \tag{3}$$

where $\hat{\mathbf{f}}(\mathbf{y})$ is force per unit area and Σ denotes the surface of the fiber. As the regularization parameter ε approaches zero, the kernel S_ε approaches the classical singular Stokeslet S_0.

We nondimensionalize this coupled fluid-fiber problem by choosing a characteristic length scale $\mathcal{L} = \hat{L}_0$ on the order of a fiber length, a time scale $\mathcal{T} = \alpha\dot{\gamma}^{-1}$, a velocity scale $\mathcal{U} = \hat{L}_0/\mathcal{T}$, and a force scale $\mathcal{F} = \mu\hat{L}_0^2/\mathcal{T}$. Here α is a non-dimensional tuning parameter for background shear flow that is chosen to be $\alpha = 2.5$ in all simulations shown below. We will use these non-dimensionalized quantities throughout the manuscript.

2.2. Representation of fiber

The model fiber that we consider has a native straight shape and equilibrium length L. We construct the discretization of the surface of the cylindrical fiber by placing cross-sections of radius R_f along the centerline, perpendicular to the centerline (see Fig. 1). Each cross-section is discretized by $N_c = 18$ points, and we take N_f cross-sections along the fiber so that the spacing between neighboring cross-sections is approximately equal to the spacing between adjacent points on a cross section.

Each of the $N = N_c \times N_f$ discrete points on the surface of the fiber is connected to a subset of the other surface points by a Hookean spring, giving elasticity to the structure. We define the elastic energy in the system as

$$\mathcal{E} = \frac{1}{2} \sum_j k_j l_j \left(\frac{\|\mathbf{x}_{j_1} - \mathbf{x}_{j_2}\|}{l_j} - 1 \right)^2 \tag{4}$$

where k_j is the stiffness of a spring with resting length l_j that connects points j_1 and j_2. The sum is over all springs. The force at $\mathbf{x}_{j_1}$ is $\mathbf{f}_{j_1} A_{j_1}$ where A_{j_1} is the area of a patch of surface centered at $\mathbf{x}_{j_1}$ in the discretization. The elastic forces are derived from the energy function:

$$\mathbf{f}_{j_1} A_{j_1} = -\frac{\partial \mathcal{E}}{\partial \mathbf{x}_{j_1}}$$

This network of nodes and elastic linkages will impart tensile stiffness and bending rigidity to the fiber, calibrated by the connectivity of the nodes and the stiffness constants of individual linkages. Similar constructs of semi-flexible filaments coupled to an incompressible fluid have been used to model bacterial flagella [5,11,12] and diatom chains [18]. In all simulations shown here, we choose a network connectivity so that each point on a given cross-section is connected to every other
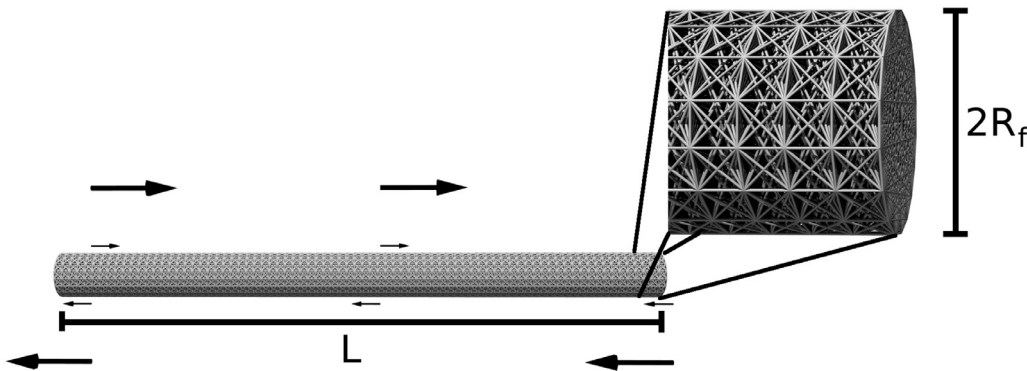

Fig. 1. Fiber model consisting of points on fiber surface connected by a network of springs. The inset shows more detail of the spring network comprising the fiber. The arrows indicate the background shear flow. The fiber shown here has $N_f = 80$ cross-sections and $N_c = 18$ nodes per cross section.

Table 1

Geometric and material parameters of fibers and numerical parameters (all non-dimensional).

Quantities	Dimensionless value
Fiber length, L	0.139–2.28
Fiber radius, R_f	0.005
Slenderness ratio, $\rho = R_f/L$	0.0022–0.036
Spring stiffness, k	0.0112
Bending rigidity, EI	4.8×10^{-6}
Shear scale, α	2.5
Elasto-viscous number, $\bar{\mu}$	$5.35 \times 10^2 - 2.37 \times 10^7$
Numerical Parameters	
Cross sections along fiber, N_f	80–1313
Points per fiber cross section, N_c	18
Total number of points on fiber N	1440–23634
Spacing between fiber nodes, Δs	0.00174
Blob size, ε	0.00225
Time step, Δt	1.0×10^{-4}

point on that cross-section, as well as to every other point on the two cross-sections adjacent to it. This means that each node is connected to $17 + 2 \times 18 = 53$ other nodes. In addition, in all simulations shown, the stiffness constant $k_j = k$ in Eq. (4) is taken to be the same for all springs. The resting lengths of the springs, l_j in Eq. (4) do vary with j, and are determined by the straight fiber configuration.

Due to the imposed background shear, the flexible fiber will depart from its equilibrium shape as the network springs become stretched or compressed, causing forces at the nodes to develop. The fluid velocity due to these elastic forces is evaluated at each material point $\mathbf{x}_i, i = 1, \ldots, N$ of the fiber surface, using a discrete version of (Eq. (3)):

$$\mathbf{u}_{st}(\mathbf{x}_i) = \sum_{j=1}^{N} S_\varepsilon(\mathbf{x}_i, \mathbf{x}_j)\mathbf{f}_j A_j.$$

Using the forward Euler method, this velocity, added to the background shear velocity $\mathbf{u}_b$, is used to update the positions of the nodes of the flexible fiber. The range of the fiber's (non-dimensional) geometrical and elastic parameters used in simulations are shown in Table 1, along with the numerical parameters used. An efficient alternative treatment of the surface integration is to use boundary elements. Such an approach was used by Smith [23] for computing flows generated by cilia and flagella.

2.3. Calculation of fiber bending rigidity and non-dimensionalization

The macroscopic bending rigidity EI of the node-spring structure depends upon the individual spring constants k_j and the topology of the spring network. We assume that the fiber is an Euler-Bernoulli beam that is intrinsically straight. The bending energy stored in such a beam, whose centerline is given by $\mathbf{X}(\mathbf{s})$, is:

$$\mathcal{E} = \frac{EI}{2} \int_0^L \left\| \frac{\partial^2 X}{\partial s^2} \right\|^2 ds. \tag{5}$$

For a fiber of length L that is bent into a circular arc with a prescribed curvature κ, the energy in Eq. (5) is:

$$\mathcal{E} = \frac{EI}{2} \kappa^2 L. \tag{6}$$

In our node-spring formulation, we can directly calculate the bending energy for a given bent configuration by using Eq. (4) which gives us the energy in the spring network. Exploiting this, as in [12,18], we can precompute the bending rigidity EI of one of our computational fibers by bending it into a circular arc of curvature κ. Because this curved shape stretches and compresses the network of springs, a non-zero elastic energy $\mathcal{E}$ emerges. Finally, we use Eq. (6) to solve for the bending rigidity EI.

As in other elastohydrodynamic systems where flexible fibers are coupled to a Stokesian incompressible fluid, the dynamics are governed by two non-dimensional parameters: the fiber aspect ratio (slenderness parameter) $\rho = R_f/L$, and the elasto-viscous number that measures the relative importance of flow forces to elastic forces (e.g., [14,18,24,25,27]). We define the elasto-viscous number:

$$\bar{\mu} = \frac{8\pi\mu\dot{\gamma}\hat{L}^4}{c\hat{E}\hat{I}} = \frac{8\pi\alpha L^4}{cEI},$$

where we have indicated the ratio both in dimensional parameters and using our non-dimensional scaling. For a given slenderness ratio ρ, the tangential drag on the filament is given by the geometric parameter $c = \ln(4e/\rho^2)$. Moreover, in this work, we do not consider the effect of thermal fluctuations.

3. Using mixed kernels in kernel independent FMM for regularized Stokeslet

3.1. Kernel independent FMM steps

During the solution of the fiber dynamics, the velocity of each node on the fiber must be evaluated at every time step. The direct evaluation of the equation

$$\mathbf{u}(\mathbf{x}_i) = \sum_{j=1}^{N} S_\varepsilon(\mathbf{x}_i, \mathbf{x}_j)\mathbf{w}_j. \tag{7}$$

requires $O(N^2)$ operations. The cost can be reduced to $O(N)$ operations with the Kernel Independent Fast Multipole Method (KIFMM) [28], which builds an adaptive octree for a given set of source (S) points $\mathbf{x}_j$ and target (T) points $\mathbf{x}_k$, $1 \le k \le N$, by recursively refining the octree with no more than N_{leaf} points in each leaf box. The nomenclature used in the KIFMM is summarized in Table 2.

The interactions between points in a leaf box and other points are divided into near-field and far-field. Near-field interactions refer to points in all adjacent leaf boxes and are summed directly. Far-field interactions refer to points in non-adjacent leaf boxes and are approximated using a set of equivalent points with source strength $\mathbf{w}_k^{equiv}$ on each equivalent point k. In three dimensions, the equivalent points are chosen to be on a uniform cubic surface mesh surrounding each octree box, with p points along each cubic edge. The total number of equivalent points is $6(p-1)^2 + 2$. This approximation converges exponentially with increasing number p. The contribution from near- and far-fields are added together to form $\mathbf{u}$ at each target point.

The tradeoff between cost and accuracy is controlled by p. In general, $p = 10$ gives single-precision accuracy and $p = 16$ gives double precision accuracy. N_{leaf} controls the depth of the octree, and thus affects the total computation time. In practice, N_{leaf} is set to about 2000 to fit the current CPU architecture.

There are two ways to invoke the KIFMM for S_ε. The first choice is to directly use $S_\varepsilon \in \mathcal{R}^{3\times3}$ as the kernel for all operations throughout the octree, for both near-field and far-field interactions. This approach is straightforward to implement, but is limited to a common value of ε for all points. Further, if periodic boundary condition are necessary, the periodizing operator $\mathcal{T}_{M2L}$ must be recalculated for each different ε [26]. Another approach is to regard each source point in S_ε as a four dimensional vector ($w_1, w_2, w_3, \varepsilon$). In this case, S_ε becomes a nonlinear kernel

Table 2

Nomenclature for KIFMM to compute Eq. (7).

S_ε	regularized Stokeslet kernel
S_0	singular Stokeslet kernel
$\mathbf{w}_j = \mathbf{f}_j A_j$	the source strength at source point j
$\mathbf{w}_k^{equiv}$	the equivalent source strength at equivalent point k
p	the number of equivalent points along each cubic box edge
N_{leaf}	the maximum number of points per leaf box

because ε appears nonlinearly in S_ε. The near-field interactions between source-target pairs are computed directly. For far-field interactions, the singular kernel S_0 is used for equivalent points, and the strength $\mathbf{w}_k^{equiv}$ is found by matching the equivalent flow field with the regularized flow field generated by source points. It is straightforward to find the equivalent $\mathbf{w}_k^{equiv}$ and the exponential convergence of KIFMM is maintained because the regularized kernel S_ε is a solution to the Stokes equation. After $\mathbf{w}_k^{equiv}$ is found, the singular kernel S_0 is used throughout the tree traversal. This approach allows the regularization parameter ε to vary for different source points, and allows the direct reuse of $\mathcal{T}_{M2L}$ computed for S_0 [26] to implement various types of periodic boundary conditions.

The computation code is implemented based on the parallel KIFMM library PVFMM [15]. Both `MPI` and `OpenMP` parallelism are implemented to improve parallelization efficiency. `SIMD` instructions are also utilized to improve efficiency on modern CPU architectures.

4. Results and discussion

In recent laboratory experiments that investigate the dynamics of actin filaments in shear [14], the diameter and bending rigidity of the fibers are fixed by nature. The elasto-viscous number of the experiments is varied by either adjusting the background shear or observing actin filaments of different lengths. Motivated by these experiments, here we choose to examine the dynamics of fibers in shear by keeping their bending rigidity and their diameter fixed, but vary their length. The shear rate remains fixed in these simulations. As the fiber length increases, its slenderness ratio decreases, and the corresponding elasto-viscous number of the system increases.

Because we track the surface of the fiber rather than just its centerline, a straight fiber that is initialized with its centerline along the x-axis needs no perturbation to begin its orbit – spatial gradients in velocity on

each cross section are immediately formed. In the absence of Brownian fluctuations, the dynamics of a perfectly cylindrical fiber whose centerline initially coincided with the x-axis in this unbounded shear flow must necessarily obey some symmetry constraints. In particular, the centerline must remain in the plane that it was initialized in and the shape deformations with respect to the centroid of the fiber must be odd. In the simulations presented below, we will see the effects of the small fluctuations that occur due to the numerical perturbations that arise from time integration and from the finite discretization of the fiber surface.

Although not included here, thermal fluctuations can be included in this model by adding random forces to each node chosen from an appropriate distribution. Preliminary simulations indicate that the thermal fluctuations break the symmetry of the system, pushing all fibers out of the plane earlier in time than do the numerical fluctuations alone. The onset of this symmetry breaking depends upon the relative sizes of the noise and the background flow.

The time step Δt used for all simulations, indicated in Table 1, was chosen based upon experiments with short fibers. We sought a time-step that was small enough so that the explicit Euler integration remained stable, but one that was large enough for reasonable computational time. Identifying this time step Δt, we simulated the motion of the short fiber in shear flow using Δt, $\Delta t/2$, and $\Delta t/4$ to test convergence. The difference in the node locations after one periodic orbit was no larger than $\mathcal{O}(10^{-6})$ (the fiber length is $O(10^{-1})$). On the other hand, using $2\Delta t$ was unstable.

Fig. 2 shows the periodic orbits of three fibers of increasing length that display the signature tumble, S-turn and snaking behavior reported by [6,14,17,24]. The first column of Fig. 2 depicts the rotational orbit of a fiber of length $L = 0.139$ ($\bar{\mu} = 5.35 \times 10^2$) that exhibits little deformation from its straight shape. Fig. 3(a) shows a surface plot of the evolving (absolute value of) curvature along the arclength of the fiber
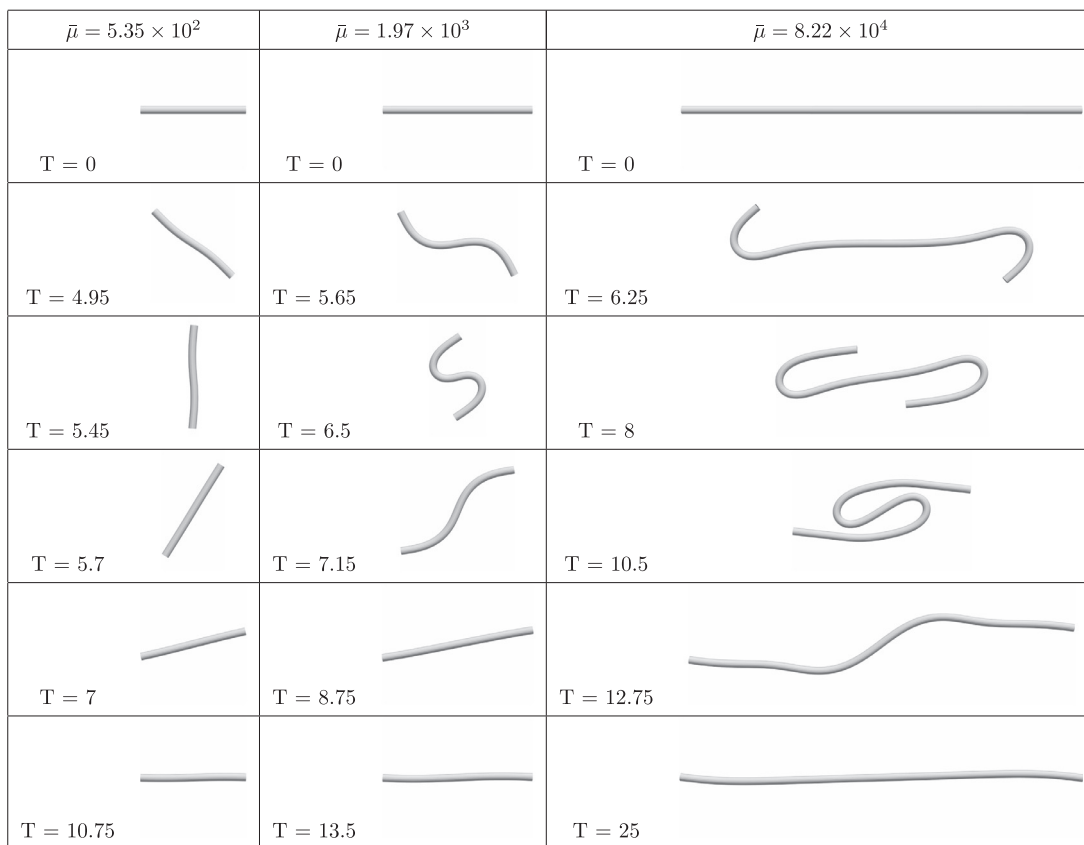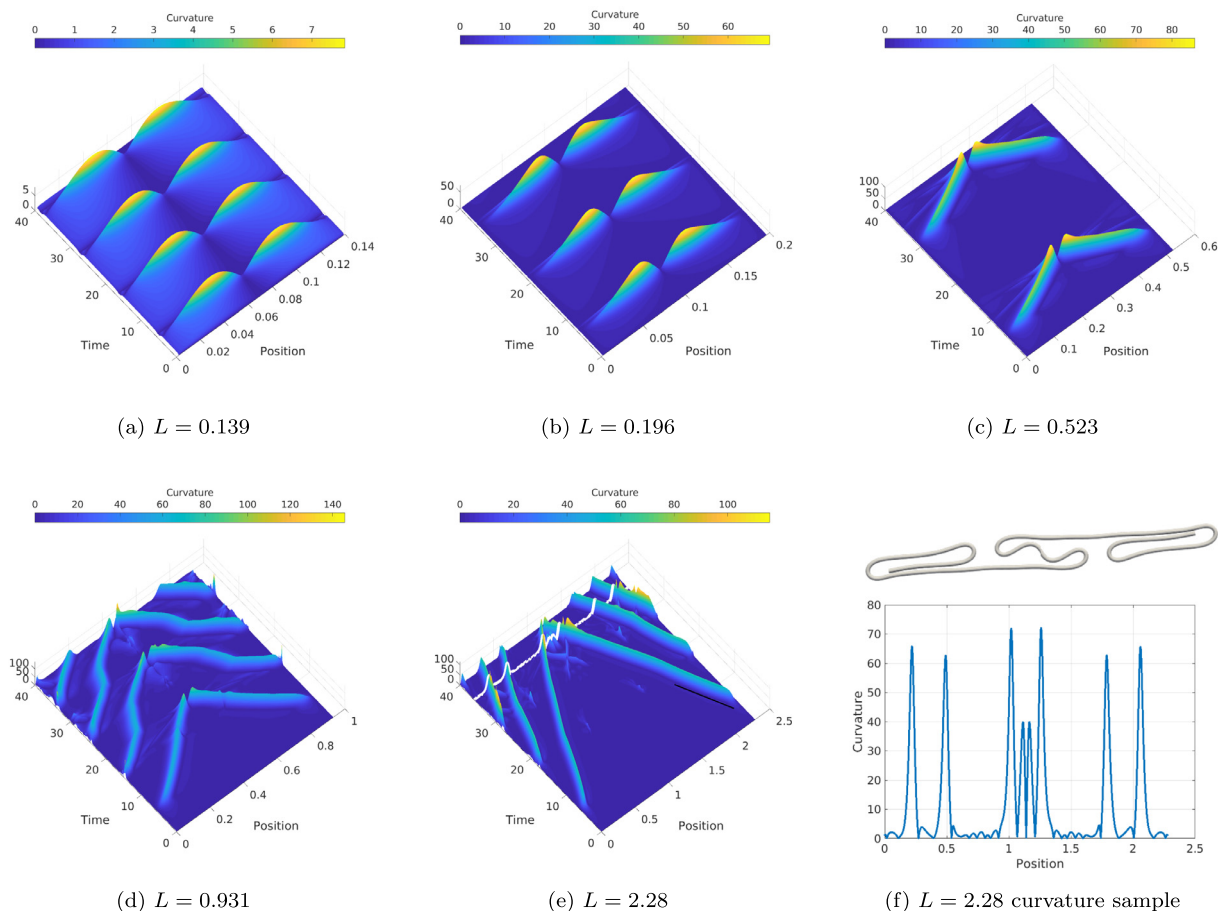

$\bar{\mu} = 5.35 \times 10^2$	$\bar{\mu} = 1.97 \times 10^3$	$\bar{\mu} = 8.22 \times 10^4$
T = 0	T = 0	T = 0
T = 4.95	T = 5.65	T = 6.25
T = 5.45	T = 6.5	T = 8
T = 5.7	T = 7.15	T = 10.5
T = 7	T = 8.75	T = 12.75
T = 10.75	T = 13.5	T = 25

Fig. 2. Fibers of lengths $L = 0.139, 0.196, 0.523$ with corresponding elasto-viscous numbers of $\bar{\mu} = 5.35 \times 10^2, 1.97 \times 10^3, 8.22 \times 10^4$ respectively. Here we see the classical tumble, S-turn, and snaking periodic orbits. These dynamics are shown in Movie S1.

Fig. 3. Surface plots of the curvature as a function of time and arclength along the fiber. Note that we are not considering signed curvature for fibers of length (a) $L = 0.139$; (b) $L = 0.196$, (c) $L = 0.523$, (d) $L = 0.931$, (e) $L = 2.28$. Shown in panel (f) is the curvature along the longest fiber $L = 2.28$ at time $T = 36$. Here multiple extrema in curvature appear and can be identified with the fibers shape also shown.

as a function of time during approximately five orbits. We see that two slight bends occur during each rotation when the fiber is aligned with the maximal compressive region of the shear (a forty-five degree angle with the negative x-axis), as in the $T = 4.95$ snapshot in the first column of Fig. 2. The positions of maximal curvature do not travel along the arclength of the fiber, but occur as standing waves that appear periodically in each orbit. The second column of Fig. 2 depicts the rotational orbit of a fiber of length $L = 0.196$ ($\bar{\mu} = 1.97 \times 10^3$) that clearly buckles into an S-shape during its orbit. Fig. 3(b) shows the corresponding evolution of curvature. Again we see standing waves of curvature. In contrast, the third column of Fig. 2 shows the snaking behavior of a fiber of length $L = 0.523$ ($\bar{\mu} = 8.22 \times 10^4$). Here the ends of the fiber curl in towards the middle of the fiber in an antisymmetric manner, and the points of maximal curvature travel along its arclength. These traveling waves of maximal curvature are evident in Fig. 3(c) during the times at which the fiber is bent from its straight configuration. In each of the simulations shown in Fig. 2, the fibers exhibit periodic orbits, and during most of the orbit the fibers remain in a nearly straight configuration aligned with the x-axis. Note that the period of rotation increases with the length of the fiber.

We compare the above with the coordinated experiments and simulations of actin fibers with Brownian fluctuations by Liu et al. [14] where the values of elasto-viscous number $\bar{\mu}$ at which transitions from tumbling to buckling to snaking occurred were quantified. The elasto-viscous numbers of the simulations presented in Fig. 2 fall squarely within the ranges of these different dynamical regimes. We note that because of the imposed symmetry in our model, in the absence of a perturbed initial

position or Brownian fluctuations, we do not observe the C-buckling or U-turns reported in [14], but rather their counterparts with odd symmetry. If perturbations were added to the initial placement of the fiber, we do observe such asymmetric shapes (not shown).

We now examine the dynamics of longer fibers with values of elasto-viscous number $\bar{\mu}$ that transition from the snaking behavior shown in the third column of Fig. 2 to more complex dynamics and shape evolution. Fig. 4 shows some time snapshots of a fiber of length $L = 0.931$ in shear with a corresponding elasto-viscous number ($\bar{\mu} = 7.51 \times 10^5$) that is beyond those considered in [14]. At time $T = 4.95$ we observe the emergence of the hooks at each end that are evident in snaking behavior. However, it is worthwhile to compare the snapshot of the $L = 0.523$ fiber in Fig. 2 at $T = 10.5$ to the longer fiber in Fig. 4 at $T = 16.25$. In the longer fiber, we see that additional hooks have formed at the ends, giving multiple local extrema in curvature along the fiber. The evolution of the curvature is shown in Fig. 3(d), where we can see the propagation of traveling waves of curvature. We remark that this fiber never did regain its straight shape. Fig. 5 shows the dynamics of an even longer fiber of length $L = 2.28$ that exhibits even richer shape dynamics. Again, the hooks appear at the fiber ends at $T = 10$, but the fiber is long enough to support multiple coils as time evolves, as well as additional buckling sites in the middle. Fig. 3(e) shows the evolution of the curvature along this fiber with a cross-section at time $T = 36$ indicated. Fig. 3(f) shows the curvature plotted at $T = 36$ as a function of arclength. The multiple peaks in curvature can be identified in the fiber configuration also shown. In Fig. 5 we can observe that at about $T = 50$, the perturbations due to numerical fluctuations cause the centerline of the fiber to move

T = 0

T = 4.95

T = 13.35

T = 16.25

T = 18.25

T = 20.3

T = 23.75

T = 25.5

T = 28

T = 30

T = 30.75

T = 31.25
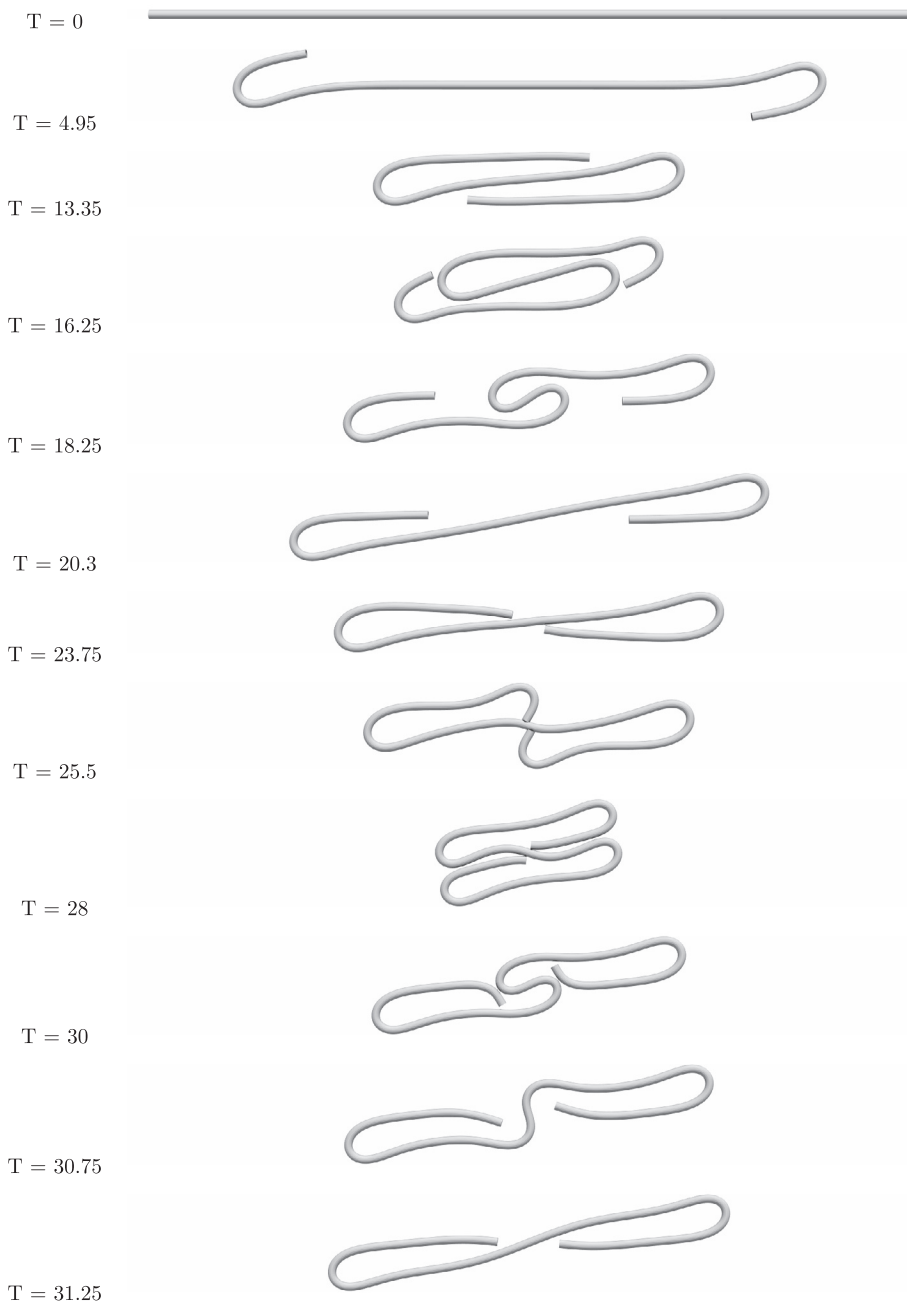
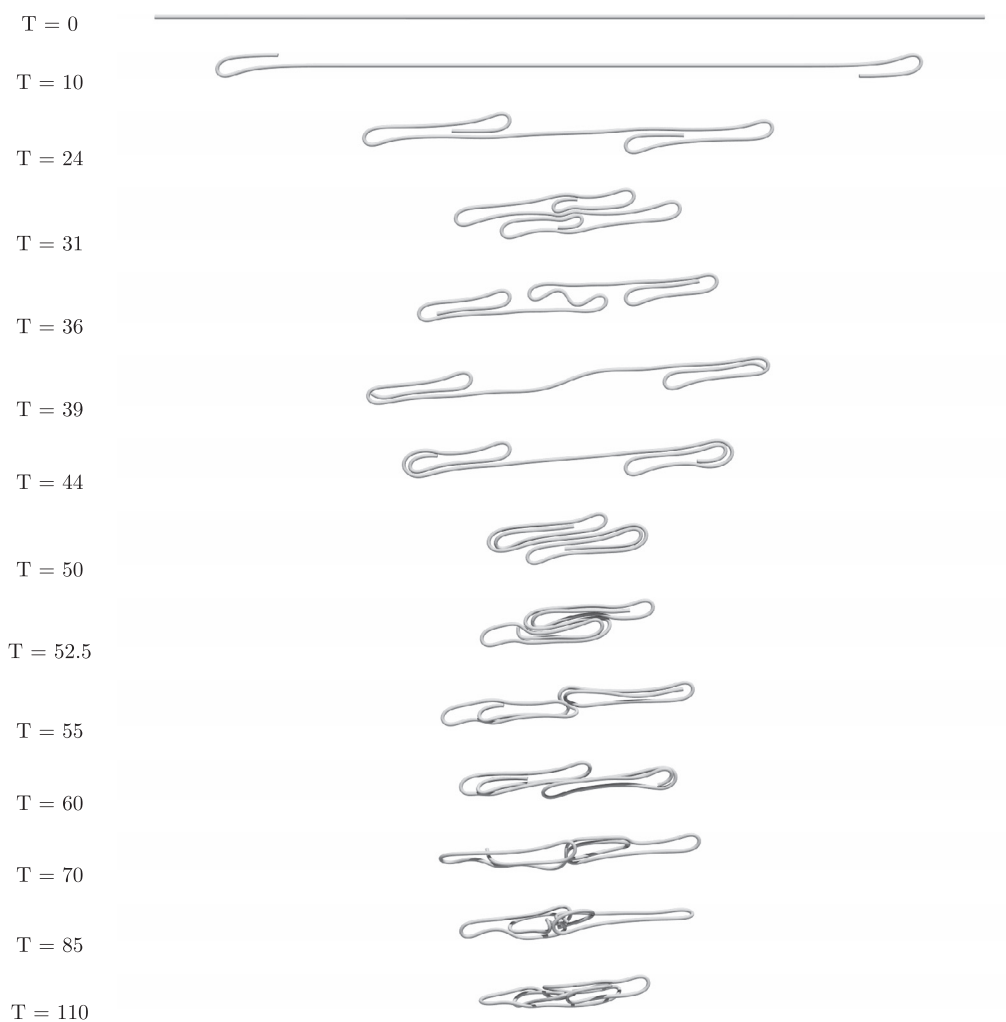**Fig. 4.** Shape deformations of a fiber of length $L = 0.931$ with corresponding elasto-viscous number $\bar{\mu} = 7.51 \times 10^5$. These dynamics are shown in Movie S2.

out of the plane, giving rise to the entanglement seen by Forgacs and Mason [6] and in [13]. Fig. 6 shows a zoomed-in image of this entanglement at time $T = 110$.

Both Harasim et al. [7] and Liu et al. [14] presented theoretical analysis of the dynamics of the J shape at the fiber ends that evolve during a snaking orbit. In particular, it was assumed that the hook developed is well-approximated by a semicircle of a fixed radius. For fibers in our simulations that did cross the threshhold of $\bar{\mu}$ at which snaking occurs, we measured the radius of such a circle using a least squares fit (see Fig. 7(a)). Even for large values of $\bar{\mu}$, the initiation of bending exhibits the emergence of hooks. Fig. 7(b) shows that the emergent radii is nearly independent of the length of the fiber and, hence, independent of $\bar{\mu}$. Because our computations are nearly at the limit of long filaments, this agrees with the predictions of [7]. During the initiation of the snaking in each of the simulations (even those that go on to complex shape deformations with no periodic orbits), we can measure the speed

of propagation of the maximal curvature along the fiber arclengths. This is equivalent to the slope of the traveling waves in the curvature surface plots in Fig. 3(c–e). Although not immediately apparent, because the range of the spatial axis is the arclength of the fiber which is different in each panel, these slopes are nearly equal. As with the hook radii, we find that these "snaking velocities" are also nearly independent of $\bar{\mu}$ (see Fig. 7(b)).

The transitions from tumbling to S-turns to snaking to complex coiling shown in Figs. 2–5 are summaried in Fig. 8. In this state diagram, we catalog the shape evolution of fibers from thirteen different simulations with fibers of increasing length. As all other parameters such as bending rigidity, fluid viscosity and background shear rate were not varied, elongating the fiber in successive simulations results in decreasing its aspect ratio and increasing the elasto-viscous number of the system. The elasto-viscous number of a simulation is indicated along the x-axis of Fig. 8. For each of the simulations, we place a vertical bar above its elasto-

Fig. 5. Shape deformations of a fiber of length $L = 2.28$ with corresponding elasto-viscous number $\bar{\mu} = 2.37 \times 10^7$. Note that after $T = 50$ the fiber centerline is no longer planar. Numerical fluctuations allow the fiber to exhibit a series of 3D coiled and entangled states. These dynamics are shown in Movie S3.
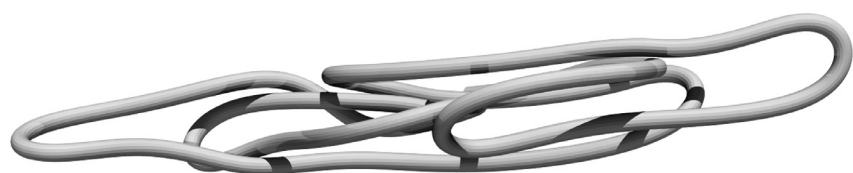
Fig. 6. A zoomed-in image at $T = 110$ of the 3D entangled state of the fiber of length $L = 2.28$ with corresponding visco-elastic number $\bar{\mu} = 2.37 \times 10^7$, This entangled image may be viewed from different directions in Movie S4.
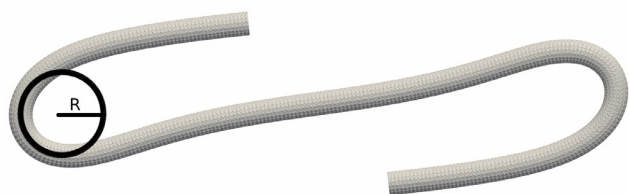
(a)
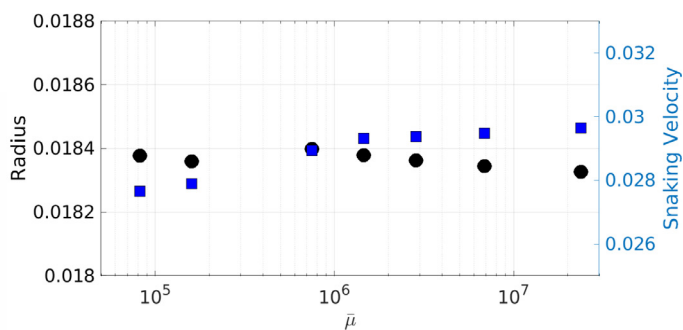
(b)

Fig. 7. (a) Radius of *J*-turn illustrated on a fiber. (b) For elasto-viscous numbers that exhibit *J*-turn formations initially, the computed radius of the hook and the snaking velocity during the initial snaking. Note that all simulations, independent of fiber length (and, hence, visco-elastic number), result in radii and velocities that are nearly constant.
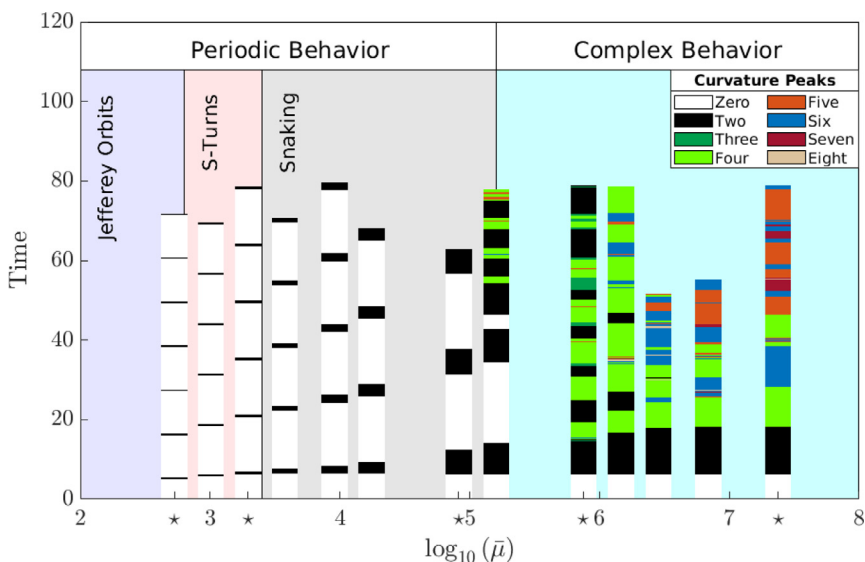
Fig. 8. A state diagram that catalogs the shape evolution of fibers from thirteen different simulations with fibers of increasing length. The elasto-viscous number of a simulation is indicated along the x-axis. For each of the simulations, we place a vertical bar above its elasto-viscous number that is color-coded to indicate the number of curvature peaks during the course of that simulation, with time increasing from bottom to top. The simulations corresponding to the snapshots shown in Figs. 2, 4, 5 are indicated with a * under their respective elasto-viscous numbers.
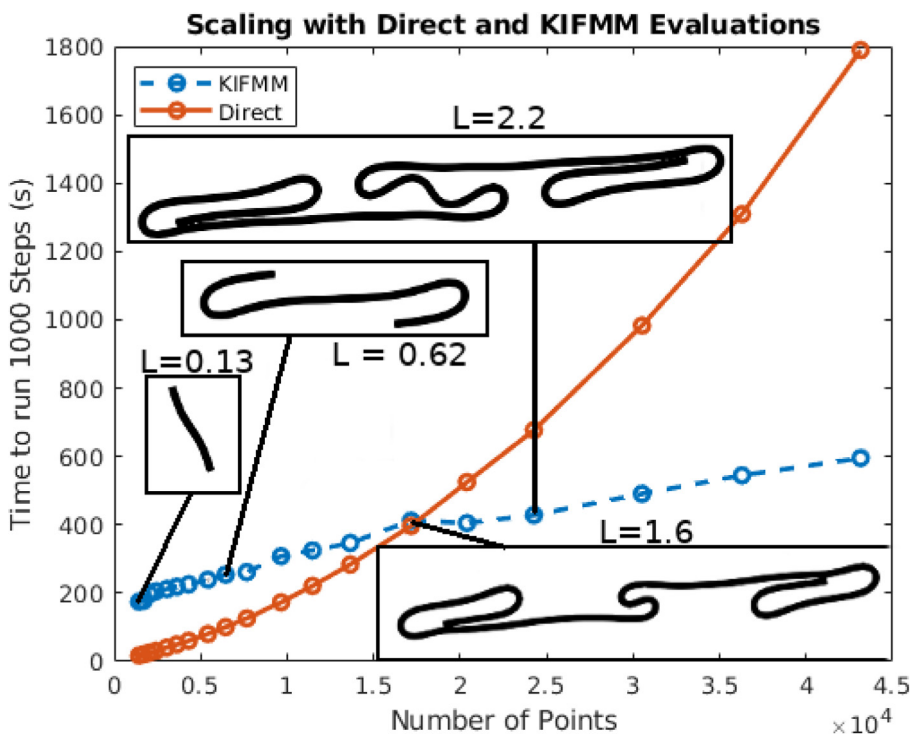

Fig. 9. Timings for regularized Stokeslet simulations using direct N^2 force evaluation and kernel independent fast multipole (KIFMM) evaluation as a function of the number of discrete points comprising the fiber surface. Note that the number of points increases as fiber length increases. The insets show a few fiber geometries at that value of N surface points.

viscous number that is color-coded to indicate the presence of curvature peaks during the course of that simulation, with time increasing from bottom to top. The simulations corresponding to the snapshots shown in Figs. 2, 4, 5 are indicated with a ⋆ under their respective elasto-viscous numbers. For fibers of all lengths, we see that the initial peaks occur at approximately the same time $T_0 \approx 5$. Note that even for the shortest fiber shown in the first column of Fig. 2, a slight S-shape bend develops in the most compressive region, but quickly dissipates. The right-most vertical bar in Fig. 8 shows this periodic behavior, where the black dash indicates the two curvature peaks along the ever-so-slightly bent fiber with odd symmetry.

We placed the transition from tumbling to S-shape near this elasto-viscous number. As the fiber lengths move from the *S*-turn region (where the duration of the two curvature peaks is short), to be long enough to propagate a snake turn, we see that the fiber supports two curvature

peaks for a longer duration of time, indicated by the height of the black bars. This duration increases with fiber length. For the snaking fibers, the curvature wave has to travel approximately half the length of the fiber at the approximately constant snaking speed shown in Fig. 7. Thus, the duration of the curvature peaks increases linearly with fiber length in this snaking region.

Up until an elasto-viscous number of about 10^5, these non-Brownian fibers exhibit periodic motion and their centerlines are confined to a plane. We do see a transition to complex behavior, indicted in Fig. 8, where this periodic behavior is lost, and the fiber supports more than two curvature peaks. We remark that, until numerical fluctuations break the symmetry of the system, there must be an even number of curvature peaks along a fiber. This symmetry breaking is, indeed, observed for large elasto-viscous numbers. In this region of complex behavior, the vertical bars corresponding to the fibers shown in Fig. 4 and 5 indicate

that the fibers evolve from a two to a four curvature peak configuration as they develop bends in their middle (i.e., $T = 16.25$ in Fig. 4) or develop a second *J*-turn at each end (i.e., $T = 24$ in Fig. 5). After a second *J*-turn has formed at the ends, the fiber will further interact with itself, and more curvature peaks can develop (i.e., at $T = 60$ in Fig. 5 we see six such peaks). The motion of these long, flexible fibers exhibit a wealth of dynamics including symmetry-breaking and entanglements.

4.1. Computational considerations

To capture the complex coiling and entanglement dynamics of slender fibers, fine resolution of their surface and along their length is required. While the regularized Stokeslet formulation relies on fundamental solutions of the Stokes equations and not a finite difference or finite element discretization of the surrounding three-dimensional fluid domain, a direct N^2 evaluation of N velocities at N nodes becomes prohibitive for large N. Fig. 9 presents the timings for 1000 time steps of the fiber-fluid system using direct summation and KIFMM summation. We see that for small fiber lengths, the overhead for KIFMM outweighs its benefits, but that a cross-over occurs at about $N = 1.7 \times 10^4$ nodes, corresponding to a fiber length of $L = 1.6$. For the longest fiber of length $L = 2.2$ we already see a factor of 1.6 speed-up. This speed-up will be significant for simulations of multiple fiber dynamics.

Note that in the simulations presented above, and in the entangled state shown in Fig. 6, there is no self-intersection of the fiber. Because of finite time steps and finite regularization parameters, we cannot rule out self-intersection. While we have not implemented any repulsive forces as fiber points get very close, such adjustments to the algorithm can be included.

5. Conclusions

In summary, we have presented a computational method that captures complex shape deformations of long flexible fibers in shear. Using the method of regularized Stokeslets in conjunction with a kernel independent fast multipole method we are able to simulate the dynamics of fibers at elasto-viscous numbers that are a couple of orders of magnitudes larger than those reported using slender body formulations. Because the fiber is represented by a spring-node system with individual spring elements, it is straightforward to model fibers with inhomogenous material properties by altering connectivities and stiffness constants of the individual elements. Moreover, the implementation of KIFMM will allow us to probe the interaction of multiple fibers in an array of background flows beyond a simple linear shear.

Acknowledgements

Supplementary material

Supplementary material associated with this article can be found, in the online version, at doi:10.1016/j.jnnfm.2019.06.007.

References

[1] R. Cortez, L. Fauci, A. Medovikov, The method of regularized Stokeslets in three dimensions: analysis, validation, and application to helical swimming, Phys. Fluids 17 (3) (2005) 031504.
[2] R. Cortez, The method of regularized Stokeslets, SIAM J. Sci. Comput. 23 (4) (2001) 1204–1225.
[3] O. du Roure, A. Lindner, E. Nazockdast, M. Shelley, Dynamics of flexible fibers in viscous flows and fluids, Ann. Rev. Fluid Mech. 51 (2019) 539–572.
[4] L. Fauci, R. Dillon, Biofluid mechanics of reproduction, Annu. Rev. Fluid. Mech. 38 (2006) 371–394.
[5] H. Flores, E. Lobaton, S. Méndez-Diez, S. Tlupova, R. Cortez, A study of bacterial flagellar bundling, Bull. Math. Biol. 67 (1) (2005) 137–168, doi:10.1016/j.bulm.2004.06.006.
[6] O. Forgacs, S. Mason, Particle motions in sheared suspensions: X Orbits of flexible threadlike particles, J. Colloid Sci. 14 (1959) 473–491.
[7] M. Harasim, B. Wunderlich, O. Peleg, M. Kroger, A. Bausch, Direct observation of the dynamics of semiflexible polymers in shear flow, Phys. Rev. Lett. 110 (2013) 108302.
[8] V. Kantsler, R. Goldstein, Fluctuations, dynamics, and the stretch-coil transition of a single actin filament in extensional flow, Phys. Rev. Lett. 108 (2012) 038103.
[9] L. Karp-Boss, P.A. Jumars, Motion of diatom chains in steady shear flow, Limnol. Oceanogr. 43 (8) (1998).
[10] S. Kuei, A.M. Słowicka, M.L. Ekiel-Jeżewska, E. Wajnryb, H.A. Stone, Dynamics and topology of a flexible chain: knots in steady shear flow, New J. Phys. 17 (5) (2015) 053009.
[11] J. LaGrone, R. Cortez, L. Fauci, Elastohydrodynamics of swimming helices: effects of flexibility and confinement, Phys. Rev. Fluids 4 (2019) 033102, doi:10.1103/Phys-RevFluids.4.033102.
[12] S. Lim, C. Peskin, Simulations of the whirling instability by the immersed boundary method, SIAM J. Sci. Comp. 25 (6) (2004) 2066–2083.
[13] Y. Liu, Dynamics of Flexible and Brownian Filaments in Viscous Flows, l'Universite Paris Diderot, 2018 Ph.D. thesis.
[14] Y. Liu, B. Chakrabarti, D. Saintillan, A. Lindner, O. du Roure, Morphological transitions of elastic filaments in shear flow, Proc. Natl. Acad. Sci. 115 (38) (2018) 9438–9443.
[15] D. Malhotra, G. Biros, PVFMM: a parallel kernel independent FMM for particle and volume potentials, Commun. Comput. Phys. 18 (03) (2015) 808–830, doi:10.4208/cicp.020215.150515sw.
[16] H. Manikantan, D. Saintillan, Buckling transition of a semiflexible filament in extensional flow, Phys.Rev. Lett. 92 (2015).
[17] F. Nguyen, M. Graham, Buckling instabilities and complex trajectories in a simple model of uniflagellar bacteria, Biophys. J. 112 (5) (2017) 1010–1022, doi:10.1016/j.bpj.2016.12.051.
[18] H. Nguyen, L. Fauci, Hydrodynamics of diatom chains and semiflexible fibres, J. Royal Soc. Interface 11 (2014) 20140314.
[19] L. Pieuchot, J. Lai, R. Loh, F. Leong, K.-H. Chiam, G. Stajich, G. Jedd, Cellular subcompartments through cytoplasmic streaming, Devel. Cell 34 (2015) 410–420.
[20] C. Pozrikidis, Boundary Integral and Singularity Methods for Linearized Viscous Flow, Cambridge Texts in Applied Mathematics, Cambridge University Press, 1992.
[21] N. Quennouz, M. Shelley, O. du Roure, A. Lindner, Transport and buckling dynamics of an elastic fibre in a viscous cellular flow, J. Fluid Mech. 769 (2015) 387–402.
[22] M. Shelley, The dynamics of microtubule/motor-protein assemblies in biology and physics, Ann. Rev. Fluid Mech. 48 (2016) 487–506.
[23] D.J. Smith, A boundary element regularized Stokeslet method applied to cilia- and flagella-driven flow, Proc. R. Soc. London A 465 (2112) (2009) 3605–3626, doi:10.1098/rspa.2009.0295.
[24] A. Tornberg, M. Shelley, Simulating the dynamics and interactions of elastic filaments in Stokes flow, J. Comp. Phys. 196 (2007) 8–40.
[25] E. Wandersman, N. Quennouz, M. Fermigier, A. Lindner, O. du Roure, Buckled in translation, Soft Matter 6 (2010) 5715–5719.
[26] W. Yan, M. Shelley, Flexibly imposing periodicity in kernel independent FMM: a multipole-to-local operator approach, J. Comput. Phys. 355 (Supplement C) (2018) 214–232, doi:10.1016/j.jcp.2017.11.012.
[27] Q. Yang, L. Fauci, Dynamics of a macroscopic elastic fibre in a polymeric cellular flow, J. Fluid Mech. 817 (2017) 388–405.
[28] L. Ying, G. Biros, D. Zorin, A kernel-independent adaptive fast multipole algorithm in two and three dimensions, J. Comput. Phys. 196 (2) (2004) 591–626, doi:10.1016/j.jcp.2003.11.021.